Journal of Sound and Vibration 329 (2010) 1653–1672

Contents lists available at ScienceDirect

Journal of Sound and Vibration

journal homepage: www.elsevier.com/locate/jsvi

An alternative to modal analysis for material stiffness and damping identification from vibrating plates

Alain Giraudeau *, Fabrice Pierron, Baoqiao Guo

Laboratoire de Mécanique et Procédés de Fabrication, Arts et Metiers ParisTech, Rue Saint-Dominique, BP 508, 51006 Châlons-en-Champagne Cedex, France

ARTICLE INFO

Article history:
Received 13 July 2009
Received in revised form
18 November 2009
Accepted 25 November 2009
Handling Editor: C.L. Morfey
Available online 30 December 2009

ABSTRACT

This paper presents an alternative to modal analysis to extract stiffness and damping parameters from thin vibrating plates. Full-field slope measurements are performed through a deflectometry technique on a plate vibrating at a given frequency. Images are recorded in phase and at $\pi/2$ lag from the excitation. From this information, deflection fields are computed by integration and curvature fields are obtained by differentiation. This information is then input into the principle of virtual work to extract both stiffness and damping parameters. This procedure, known as the Virtual Fields Method, is detailed in the paper and the notion of special optimized virtual fields is extended to the present problem. Validation on simulated data is performed before moving to experimental data. One of the main advantages of this technique is that it is completely insensitive to the damping coming from the boundary conditions. This is illustrated experimentally on two tests where a viscoelastic layer and rubber washers are added in the experimental set up.

1. Introduction

The identification of material elastic stiffness and damping parameters, essential for the prediction of the vibrating or vibro-acoustic behaviour of a large range of structures, is common in material testing laboratories.

The identification of the stiffness parameters is usually performed using tension, bending or torsion tests on rectangular coupons leading to simple stress states that can be expressed as functions of the specimen geometry and the applied load through a closed-form solution of the mechanical problem. Nevertheless, these procedures exhibit certain drawbacks. First, experimental boundary conditions must comply with that of the mechanical model, which is not always easy to achieve. Then, only a small number of parameters can be retrieved from a specific test because of the very simple stress state. As a result, several tests have usually to be performed to identify the full set of material parameters, increasing the cost of the procedure.

As an alternative, several authors have tried to use modal data to identify the full stiffness tensor. Different approaches have been used, either analytical or numerical. Usually, the first 10–15 resonance frequencies of a thin plate in bending are considered and the analytical or numerical model updated until the experimental frequencies match that of the model [1–11]. An extension to thick plates with transverse shear was also developed [12,13]. More recently, the above approach was refined by using not only modal frequencies but also mode shapes. This resulted in more robust identification, particularly for the through-thickness shear moduli and Poisson's ratio [14–16].

* Corresponding author. Tel.: +33 326699112; fax: +33 326699176.
E-mail address: alain.giraudeau@chalons.ensam.fr (A. Giraudeau).

0022-460X/$ - see front matter © 2009 Elsevier Ltd. All rights reserved.
doi:10.1016/j.jsv.2009.11.031

An alternative to these methods was suggested by Grédiac et al. making use of the measurement of slope fields at the surface of bent plates [17–19] and performing the identification through the so-called Virtual Fields Method (VFM) which is a particular application of the principle of virtual work. The main advantage of this technique is that stiffnesses are obtained directly (no iterations, no optimization scheme) and that restrictions on specimen geometry and boundary conditions are less critical than with other methods since it does not rely on any sort of closed form or approximate solution of a forward problem. Batista et al. [20] present a particular extension of this method using isotropic modes extracted from the deflection of bent plates measured with a scanned laser Doppler vibrometer over a large number of points on the plate surface.

The identification of damping parameters is a more complex problem than stiffness because of all the parasitic dissipation that is usually added in a classical mechanical test. Most of the studies dedicated to the measurement of material damping are based on the vibrations of beams. A usual strategy consists in monitoring the vibrations of beams in free vibrations, either in bending with free–free or cantilever boundary conditions [21–26], in torsion [27,28] or in longitudinal vibrations [29]. The results are processed using either the logarithmic decay time when the first mode is predominant [21,22,24–26,28] or the half-power bandwidth of the frequency response function when several modes are present [30,31]. Other techniques such as circle-fit in the Argand plane can also be found [32]. Some authors prefer to work on forced vibrating beams using inertial excitation [33] or clamped–clamped beams with mid-span loading [34]. In any case, the experimental problems encountered by the authors are often similar: dissipation coming from the boundary conditions [22,25], presence of higher order modes [24].

The main disadvantages of working with beams is that generally, only a limited range of frequencies can be explored (corresponding to the first mode of the beam) and that for anisotropic materials, only one damping parameter can be obtained at a time and damping associated to Poisson's ratio is very difficult to retrieve. This is very important for polymer science where techniques to identify the complete set of complex stiffnesses are still wanting [35]. A very interesting procedure was proposed by Woodhouse et al. [36,37] on plates based on the analysis of the frequencies, mode shapes and vibration decay. Unfortunately, the damping factors could not be obtained very accurately because of a number of limitations among which the dissipation introduced by the supports of the free plate and the rather crude mode shape measurements but the approach was quite original and potentially powerful. Following a similar idea but with a finite element updating approach, De Visscher et al. [38] and Matter et al. [39] used a modal analysis based approach to successfully extract material damping and stiffness. However, there are a few drawbacks to such an approach. First, since it relies on mode extraction, some requirements are necessary (such as rather low damping and the fact that only resonance frequencies can be considered). Moreover, the loudspeaker excitation in free–free conditions is not convenient for larger structures. Finally, the procedure is rather heavy, with extraction of a great number of modes and the inverse problem rather computationally intensive. The fact that several modes over a large range of frequencies are needed is also a major drawback to identify the frequency dependance of damping.

The present work can be seen as an extension of the work by Grédiac et al. [17] allowing the extraction of damping parameters as well as stiffnesses with the Virtual Fields Method applied to thin plates in forced vibrations. Its principle has already been reported in [40] but the presentation here is both simpler and more general. Early experimental results were reported in [41]. Here, special and optimized virtual fields [42] are adapted to the present problem and the independence of the identified damping parameters to the boundary conditions is illustrated experimentally.

2. General problem statement

2.1. Theoretical configuration

In order to develop the method, an isotropic specimen of any shape and boundary conditions is considered. A particular area of interest, called Ω is observed. This area is delimited by a fictitious closed line Γ of any shape. Because of the surface nature of most of the full-field deformation measurement techniques, this area of interest must comply to the assumptions of Love–Kirchhoff's thin plate theory (see Fig. 1). It must also be free of any external load. Some loading device

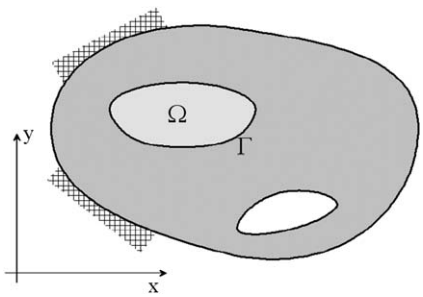

Fig. 1. Generic specimen.

acting outside Ω imposes an harmonic excitation which results in a vibrating response in pure bending of this observed area. Assuming a linear behaviour for the tested material, the bending response of Ω is harmonic at the same frequency.

It must be kept in mind that the proposed method is based on the three fundamental hypothesis presented above and recalled below:

- Love–Kirchhoff's thin plate theory;
- pure harmonic bending;
- linear behaviour.

2.2. Harmonic response

Assuming the three above items, the absolute out-of-plane displacement of any point (x,y) of Ω can be described by the harmonic time dependant function $w(x,y,t)$. According to the modal scheme, this deflection can be written as a combination of the response of each mode:

$$w(x,y,t)=\sum_{k=1}^{\infty}\lambda_k(x,y,t) \tag{1}$$

where $\lambda_k(x,y,t)$ is the contribution of the k th mode to the vibrating response. Assuming a linear viscoelastic behaviour for the material, the vibrating response of Ω is pure harmonic bending at the same angular frequency ω:

$$w(x,y,t)=\sum_{k=1}^{\infty}|\lambda_k(x,y)|\cos(\omega t-\varphi_k(x,y)) \tag{2}$$

where $|\lambda_k(x,y)|$ and $\varphi_k(x,y)$ are, respectively, the amplitude and the phase of the response of the k th mode. In the general case, a correct representation of the harmonic response of Ω must take into account the contributions of a great number of modes. This number depends if the excitation frequency is close or not to a resonance and if the modal frequencies are well separated or not [43].

On the other hand, from an observer point of view, the out-of-plane displacement of each point (x,y) of Ω can be described by

$$w(x,y,t)=\overline{w(x,y)}\cos(\omega t-\phi(x,y)) \tag{3}$$

where $\overline{w(x,y)}$ and $\phi(x,y)$ are, respectively, the amplitude field and the phase field of the bending response of Ω at the ω angular excitation frequency. This can be written as

$$w(x,y,t)=[\overline{w(x,y)}\cos\phi(x,y)]\cos\omega t+[\overline{w(x,y)}\sin\phi(x,y)]\sin\omega t=w^C(x,y)\cos\omega t+w^S(x,y)\sin\omega t \tag{4}$$

The preceding Eq. (4) shows that the deflection field can be described by its two components $w^C(x,y)$ and $w^S(x,y)$ which can be interpreted as the deflection fields observed at two instants accurately separated by a quarter of the period of the harmonic response. This expression for $w(x,y,t)$ provides a complete representation of the harmonic deflection field and is valid whether the excitation frequency is close or not to a resonance.

It must be pointed out that Eqs. (2) and (4) provide two representations of the same phenomenon, respectively, described in the modal basis and in the physical basis. It must be remarked that magnitude and phase fields $|\lambda_k(x,y)|$ and $\varphi_k(x,y)$, respectively, of the k th mode can be difficult to extract. Their knowledge needs the projection of the ω harmonic response onto the modal basis of the plate which must be first identified. On the contrary the two functions $w^C(x,y)$ and $w^S(x,y)$ can be directly measured experimentally with full-field measurement techniques [41], which is why this description will be retained in the rest of this paper.

3. The Virtual Field Method (VFM)

3.1. The principle of virtual work

The Virtual Field Method is a particular application of the principle of virtual work to the identification of mechanical material properties. For a solid S of any shape, in the case of small perturbations, the general expression of the principle of virtual work can be written as

$$-\int_V\boldsymbol{\sigma}:\boldsymbol{\varepsilon}^*\,\mathrm{d}V+\int_{\partial V}\mathbf{F}\cdot\mathbf{u}^*\,\mathrm{d}S+\int_V\mathbf{f}\cdot\mathbf{u}^*\,\mathrm{d}V=\int_V\mathbf{a}\cdot\mathbf{u}^*\,\mathrm{d}m \tag{5}$$

where $\boldsymbol{\sigma}$ is the true stress tensor, V the volume of the solid S, ∂V the surface of its boundary, $\mathbf{F}$ the surface density of external forces acting on ∂V, $\mathbf{f}$ the density of volume forces acting on V, $\mathbf{a}$ the acceleration field, $\mathrm{d}V$, $\mathrm{d}S$ and $\mathrm{d}m$ are,

respectively, the elementary volume, surface and mass. ":" represents the contracted product between two second-order tensors and " $\cdot$ " indicates the dot product between two vectors.

$\mathbf{u}^*$ is a real vector ($\mathbf{u}^* \in \mathbb{R}$) continuously defined over the whole solid and its components must be differentiable. Note that the fact that $\mathbf{u}^*$ should be zero where displacements are prescribed on the boundary (which forms the kinematic admissibility condition together with the continuous and differentiable ones) is not a necessary mathematical condition. It only filters out unknown forces from the equation with a view to forward problem solving. This condition can be partially relieved for the inverse problem so it is usually left out in the VFM. In the case of the VFM, $\mathbf{u}^*$ is user selected for the purpose of the identification and must act as a filter for the extraction of the unknown parameters.

The $\boldsymbol{\varepsilon}^*$ tensor is simply related to $\mathbf{u}^*$ such that $\varepsilon^*_{ij} = (1/2)(\partial(\mathbf{u}^*)_i/\partial x_j + \partial(\mathbf{u}^*)_j/\partial x_i)$.

In many applications of the principle of the virtual work, the $\mathbf{u}^*$ function is considered as a virtual displacement and therefore $\boldsymbol{\varepsilon}^*$ can be considered as a virtual strain tensor. In that case the four integrals of Eq. (5) can be interpreted, from the left to the right, as the virtual work of the internal forces, the virtual work of the boundary forces, the virtual work of the volume forces and finally the virtual work of the acceleration (or inertial) forces.

The principle of virtual works is mathematically equivalent to the local equilibrium equation and simply describes the global (or integral) equilibrium of the solid at any time under the action of the four types of acting forces. At this point, it must be pointed out that the principle and its related expression presented in Eq. (5) remains true if V is only a subpart of the solid S and ∂V the external boundary of this subpart. In that case, $\mathbf{F}$ includes the junction forces acting at the boundary ∂V between V and its remainder to S (and relating to the generally unknown stress distribution at this boundary).

3.2. Application of the VFM

In the considered case, since the actuator is acting outside Ω and assuming no forces are acting on the two faces of Ω, $\mathbf{F}$ only consists in the junction forces along Γ between Ω and the remainder of the structure. Assuming the action of the volume forces $\mathbf{f}$ can be neglected, the application of Eq. (5) only to the Ω subpart leads to

$$-\int_\Omega \boldsymbol{\sigma} : \boldsymbol{\varepsilon}^* \, \mathrm{d}V + \int_\Gamma \mathbf{F} \cdot \mathbf{u}^* \, \mathrm{d}S = \int_\Omega \mathbf{a} \cdot \mathbf{u}^* \, \mathrm{d}m \tag{6}$$

Since an accurate measurement of the density of the junction forces $\mathbf{F}$ along Γ cannot be obtained in most of the cases, a virtual field $\mathbf{u}^*$ must be selected such that the second integral of Eq. (6) along the border Γ is null. Then the virtual contribution of the junction forces along this border cancels out and the above equation becomes

$$-\int_\Omega \boldsymbol{\sigma} : \boldsymbol{\varepsilon}^* \, \mathrm{d}V = \int_\Omega \mathbf{a} \cdot \mathbf{u}^* \, \mathrm{d}m \tag{7}$$

In that case, the implementation of the identification using the virtual fields method consists in replacing the stress components $\boldsymbol{\sigma}$ in the above Eq. (6) by the actual strains $\boldsymbol{\varepsilon}$ issued from the constitutive law which parameters are to be identified.

It should be noted that the general procedure described above is more or less equivalent to performing finite element model updating with input of the actual measured deflection field $w(x,y,t)$ as boundary conditions along Γ, in the same spirit as described in [44]. In quasi-static, this approach can only lead to relative values of the stiffness parameters since no force measurement is involved but in dynamics, the inertial forces act as a volume built in load cell, since the full-field kinematic measurements will give access to the acceleration field by double temporal differentiation. The same idea is currently being followed for high strain rate testing [46].

3.3. Actual strain field

Since the assumption is made that the Ω area of interest is considered as an isotropic thin plate in pure bending, the Love–Kirchhoff theory [47] applies and the true strain fields at any point (x,y,z) in Ω can be described directly from the spatial deflection field $w(x,y)$ such as

$$\varepsilon_x(x,y) = z\kappa_x, \quad \varepsilon_y(x,y) = z\kappa_y, \quad \varepsilon_s(x,y) = 2\varepsilon_{xy}(x,y) = z\kappa_s \tag{8}$$

where κ_x, κ_y and κ_s are the spatial curvature fields:

$$\kappa_x(x,y) = -\frac{\partial^2 w(x,y)}{\partial x^2}, \quad \kappa_y(x,y) = -\frac{\partial^2 w(x,y)}{\partial y^2}, \quad \kappa_s(x,y) = -2\frac{\partial^2 w(x,y)}{\partial x \, \partial y} \tag{9}$$

Since the actual deflection field $w(x,y,t)$ is described by the two parts $w^C(x,y)$ and $w^S(x,y)$ (see Eq. (4)), each curvature field is harmonic time dependent too and made of two parts presented below in vector form:

$$\begin{Bmatrix} \kappa_x(x,y,t) \\ \kappa_y(x,y,t) \\ \kappa_s(x,y,t) \end{Bmatrix} = \begin{Bmatrix} \kappa_x^C(x,y) \\ \kappa_y^C(x,y) \\ \kappa_s^C(x,y) \end{Bmatrix} \cos\omega t + \begin{Bmatrix} \kappa_x^S(x,y) \\ \kappa_y^S(x,y) \\ \kappa_s^S(x,y) \end{Bmatrix} \sin\omega t \tag{10}$$

which can be noted in condensed form:

$$\{\boldsymbol{\kappa}(x,y,t)\} = \{\boldsymbol{\kappa}^C(x,y)\}\cos\omega t + \{\boldsymbol{\kappa}^S(x,y)\}\sin\omega t \tag{11}$$

3.4. Virtual fields

The virtual displacement field $\mathbf{u}^*(x,y,z)$ can be built with the same kinematics as the actual fields such that its three components can be written as follows according to the Love–Kirchhoff theory:

$$\langle u^*(x,y,z), v^*(x,y,z), w^*(x,y,z)\rangle = \langle -z\theta_x^*(x,y), -z\theta_y^*(x,y), w^*(x,y)\rangle \tag{12}$$

where $w^*(x,y)$ is the virtual deflection field and $\theta_x^*(x,y)$ and $\theta_x^*(x,y)$ the virtual slopes fields such that

$$\langle \theta_x^*(x,y), \theta_y^*(x,y)\rangle = \left\langle \frac{\partial w^*(x,y)}{\partial x}, \frac{\partial w^*(x,y)}{\partial y}\right\rangle \tag{13}$$

Then the related virtual strain tensor $\varepsilon^*(x,y,z)$ can be written as

$$\begin{aligned}\langle \boldsymbol{\varepsilon}^*\rangle = \langle \varepsilon_x^*(x,y,z), \varepsilon_y^*(x,y,z), \varepsilon_s^*(x,y,z)\rangle &= \left\langle -z\frac{\partial^2 w^*(x,y)}{\partial x^2}, -z\frac{\partial^2 w^*(x,y)}{\partial y^2}, -2z\frac{\partial^2 w^*(x,y)}{\partial x\partial y}\right\rangle \\ &= \langle z\kappa_x^*(x,y), z\kappa_y^*(x,y), z\kappa_s^*(x,y)\rangle = z\langle \boldsymbol{\kappa}^*(x,y)\rangle\end{aligned} \tag{14}$$

where $\langle \boldsymbol{\kappa}^*(x,y)\rangle$ could be interpreted as the virtual curvature field. One can remark that all the virtual fields to be selected over Ω are driven by the unique selection of the virtual deflection field $w^*(x,y)$. It should be noted also that because of the above, the virtual displacement field $w^*(x,y)$ has to be C^1.

3.5. Virtual work of internal forces ***VWIF***

With the help of the preceding definitions, and with the in-plane stress components written in vector form, the first integral of the left-hand side term of Eq. (6) can be written as

$$\mathbf{VWIF} = -\int_\Omega \boldsymbol{\sigma} : \boldsymbol{\varepsilon}^*\,\mathrm{d}V = -\int_\Omega \langle \boldsymbol{\varepsilon}^*\rangle\{\boldsymbol{\sigma}\}\,\mathrm{d}V = -\int_\Omega z\langle \boldsymbol{\kappa}^*\rangle\{\boldsymbol{\sigma}\}\,\mathrm{d}V \tag{15}$$

Since the $\boldsymbol{\kappa}^*(x,y)$ functions are only (x,y) dependent, the last above equation can be rewritten as

$$\mathbf{VWIF} = -\int_\Omega \left[\langle \boldsymbol{\kappa}^*\rangle\left(\int_{-h/2}^{+h/2} z\{\boldsymbol{\sigma}\}\,\mathrm{d}z\right)\right]\mathrm{d}S \tag{16}$$

where h is the thickness of the Ω subpart. If a Kelvin–Voigt model is chosen to describe the viscoelastic behaviour of the tested material, then $\{\boldsymbol{\sigma}\}$ can be written as the sum of an elastic contribution and a dissipative one [48] such as

$$\{\boldsymbol{\sigma}\} = \{\boldsymbol{\sigma}^e\} + \{\boldsymbol{\sigma}^d\} = [\mathbf{Q}]\{\boldsymbol{\varepsilon}\} + [\mathbf{B}]\frac{\partial}{\partial t}\{\boldsymbol{\varepsilon}\} = z[\mathbf{Q}]\{\boldsymbol{\kappa}\} + z[\mathbf{B}]\frac{\partial}{\partial t}\{\boldsymbol{\kappa}\} \tag{17}$$

where $[\mathbf{Q}]$ and $[\mathbf{B}]$ are, respectively, the in-plane elastic stiffness matrix and the damping one such that, for an isotropic material:

$$[\mathbf{Q}] = \begin{bmatrix} Q_{xx} & Q_{xy} & 0 \\ Q_{xy} & Q_{xx} & 0 \\ 0 & 0 & (Q_{xx}-Q_{xy})/2 \end{bmatrix}, \quad [\mathbf{B}] = \begin{bmatrix} B_{xx} & B_{xy} & 0 \\ B_{xy} & B_{xx} & 0 \\ 0 & 0 & (B_{xx}-B_{xy})/2 \end{bmatrix} \tag{18}$$

Substituting the stress vector from Eq. (17) into Eq. (16), one has

$$\mathbf{VWIF} = -\int_\Omega \left[\langle \boldsymbol{\kappa}^*\rangle\left(\int_{-h/2}^{+h/2} z\left(z[\mathbf{Q}]\{\boldsymbol{\kappa}\} + z[\mathbf{B}]\frac{\partial}{\partial t}\{\boldsymbol{\kappa}\}\right)\mathrm{d}z\right)\right]\mathrm{d}S \tag{19}$$

Since neither the curvature, nor the stiffness matrices (for a homogeneous material) depend on z, then direct integration of z^2 between $-h/2$ and $h/2$ gives $h^3/12$ and the previous equation can be written as:

$$\mathbf{VWIF} = -\frac{h^3}{12}\int_\Omega \left(\langle \boldsymbol{\kappa}^*\rangle[\mathbf{Q}]\{\boldsymbol{\kappa}\} + \langle \boldsymbol{\kappa}^*\rangle[\mathbf{B}]\frac{\partial}{\partial t}\{\boldsymbol{\kappa}\}\right)\mathrm{d}S \tag{20}$$

One can see here the importance of the linear z parameterization of the virtual fields. If constant through thickness virtual fields had been selected, then the integration of z between $-h/2$ and $h/2$ would have given zero and the resulting VFM equation would have led to $0=0$, which is correct but useless.

Finally, reintroducing the time dependance of the actual curvatures, **VWIF** can be written as

$$\mathbf{VWIF} = -\frac{h^3}{12}\int_\Omega (\langle \boldsymbol{\kappa}^*\rangle[\mathbf{Q}]\{\boldsymbol{\kappa}^C\} + \omega\langle \boldsymbol{\kappa}^*\rangle[\mathbf{B}]\{\boldsymbol{\kappa}^S\})\,\mathrm{d}S\cos(\omega t) - \frac{h^3}{12}\int_\Omega (\langle \boldsymbol{\kappa}^*\rangle[\mathbf{Q}]\{\boldsymbol{\kappa}^S\} - \omega\langle \boldsymbol{\kappa}^*\rangle[\mathbf{B}]\{\boldsymbol{\kappa}^C\})\,\mathrm{d}S\sin(\omega t) \tag{21}$$

3.6. Virtual work of the acceleration forces **VWAC**

From Eq. (7) the **VWAC** term can be written as

$$\mathbf{VWAC} = \int_{\Omega} \mathbf{a}(x,y,t) \cdot \mathbf{u}^*(x,y)\,\mathrm{d}m \tag{22}$$

Since in bending, the out-of-plane deflection is at least one order of magnitude higher than the in-plane displacements, then the acceleration vector can be reduced to its out-of-plane component. Assuming the plate material is homogeneous, with a density ρ, and the vibrating response in pure bending is harmonic with a pulsation ω, then the out-of-plane component of the acceleration $a(x,y,t)$ can be written as $a(x,y,t) = -\omega^2 w(x,y,t)$. This leads to

$$\mathbf{VWAC} = -\rho h\omega^2 \int_{\Omega} w(x,y,t) w^*(x,y)\,\mathrm{d}S \tag{23}$$

which can be simply rewritten using Eq. (4):

$$\mathbf{VWAC} = -\rho h\omega^2 \int_{\Omega} w^C(x,y) w^*(x,y)\,\mathrm{d}S\cos(\omega t) - \rho h\omega^2 \int_{\Omega} w^S(x,y) w^*(x,y)\,\mathrm{d}S\sin(\omega t) \tag{24}$$

One can remark that the excitation device acting outside Ω causes an inertial excitation all over this area due to its harmonic response in bending. That provides a distributed field of forces which can be evaluated through the measurements of the two components of the deflection field $w^C(x,y)$ and $w^S(x,y)$ (see Eq. (4)).

3.7. Equations of identification

Eq. (7) represents the equilibrium of the internal and acceleration forces acting on Ω:

$$\mathbf{VWIF} = \mathbf{VWAC} \tag{25}$$

It can be rewritten with the help of Eqs. (21) and (24):

$$\begin{aligned} -\frac{h^3}{12}\int_{\Omega} (\langle \boldsymbol{\kappa}^* \rangle [\mathbf{Q}] \{\boldsymbol{\kappa}^C\} + \omega \langle \boldsymbol{\kappa}^* \rangle [\mathbf{B}] \{\boldsymbol{\kappa}^S\})\,\mathrm{d}S\cos(\omega t) - \frac{h^3}{12}\int_{\Omega} (\langle \boldsymbol{\kappa}^* \rangle [\mathbf{Q}] \{\boldsymbol{\kappa}^S\} - \omega \langle \boldsymbol{\kappa}^* \rangle [\mathbf{B}] \{\boldsymbol{\kappa}^C\})\,\mathrm{d}S\sin(\omega t) \\ = -\rho h\omega^2 \int_{\Omega} (w^C w^*)\,\mathrm{d}S\cos(\omega t) - \rho h\omega^2 \int_{\Omega} (w^S w^*)\,\mathrm{d}S\sin(\omega t) \end{aligned} \tag{26}$$

Since the preceding equation must be verified at any time, it can be split into two separate equations according to the cosine or sine time dependence, respectively:

$$\begin{aligned} \int_{\Omega} (\langle \boldsymbol{\kappa}^* \rangle [\mathbf{Q}] \{\boldsymbol{\kappa}^C\} + \omega \langle \boldsymbol{\kappa}^* \rangle [\mathbf{B}] \{\boldsymbol{\kappa}^S\})\,\mathrm{d}S &= \frac{12\rho\omega^2}{h^2} \int_{\Omega} w^C w^*\,\mathrm{d}S \\ \int_{\Omega} (\langle \boldsymbol{\kappa}^* \rangle [\mathbf{Q}] \{\boldsymbol{\kappa}^S\} - \omega \langle \boldsymbol{\kappa}^* \rangle [\mathbf{B}] \{\boldsymbol{\kappa}^C\})\,\mathrm{d}S &= \frac{12\rho\omega^2}{h^2} \int_{\Omega} w^S w^*\,\mathrm{d}S \end{aligned} \tag{27}$$

For convenience, the expansion of Eqs. (27) entails the definition of four quantities noted G_C, G_S, H_C, and H_S:

$$\begin{aligned} G_C &= \int_{\Omega} \left(\kappa_x^C(x,y)\kappa_x^*(x,y) + \kappa_y^C(x,y)\kappa_y^*(x,y) + \frac{1}{2}\kappa_s^C(x,y)\kappa_s^*(x,y) \right) \mathrm{d}S \\ G_S &= \int_{\Omega} \left(\kappa_x^S(x,y)\kappa_x^*(x,y) + \kappa_y^S(x,y)\kappa_y^*(x,y) + \frac{1}{2}\kappa_s^S(x,y)\kappa_s^*(x,y) \right) \mathrm{d}S \\ H_C &= \int_{\Omega} \left(\kappa_x^C(x,y)\kappa_y^*(x,y) + \kappa_y^C(x,y)\kappa_x^*(x,y) - \frac{1}{2}\kappa_s^C(x,y)\kappa_s^*(x,y) \right) \mathrm{d}S \\ H_S &= \int_{\Omega} \left(\kappa_x^S(x,y)\kappa_y^*(x,y) + \kappa_y^S(x,y)\kappa_x^*(x,y) - \frac{1}{2}\kappa_s^S(x,y)\kappa_s^*(x,y) \right) \mathrm{d}S \end{aligned} \tag{28}$$

Therefore the cosine time dependence equation (27) gives

$$G_C Q_{xx} + H_C Q_{xy} + \omega G_S B_{xx} + \omega H_S B_{xy} = \frac{12\rho\omega^2}{h^2} \int_{\Omega} w^C w^*\,\mathrm{d}S \tag{29}$$

and the sine one leads to

$$G_S Q_{xx} + H_S Q_{xy} + \omega G_C B_{xx} - \omega H_C B_{xy} = \frac{12\rho\omega^2}{h^2} \int_{\Omega} w^S w^*\,\mathrm{d}S \tag{30}$$

One can remark that the four quantities G_C, G_S, H_C and H_S defined in Eqs. (28) involve the "C" and "S" components of the actual curvatures, respectively, taken at two instants separated by a quarter of the period of the harmonic response. These four components simultaneously take place in the two preceding Eqs. (29) and (30) and the "C" and "S" play a symmetrical

role in the relations. Since stiffness and damping are both driving the vibrating response of the plate, it is not possible to separate these parameters only from spatial information (e.g. curvature and deflection fields). The identification needs an additional temporal information represented by the components of these fields at these two particular instants.

3.8. Linear system of identification

The selection of two independent virtual fields, $u^*_{(1)}$, $u^*_{(2)}$ and their related second derivatives $\kappa_x^{*(1)}$, $\kappa_x^{*(2)}$, $\kappa_y^{*(1)}$, $\kappa_y^{*(2)}$, $\kappa_s^{*(1)}$ and $\kappa_s^{*(2)}$ leads to a linear system of four equations which unknowns are the parameters to identify Q_{xx}, Q_{xy}, B_{xx}, and B_{xy}:

$$\begin{bmatrix} G_C^{(1)} & H_C^{(1)} & \omega G_S^{(1)} & \omega H_S^{(1)} \\ G_S^{(1)} & H_S^{(1)} & \omega G_C^{(1)} & -\omega H_C^{(1)} \\ G_C^{(2)} & H_C^{(2)} & \omega G_S^{(2)} & \omega H_S^{(2)} \\ G_S^{(2)} & H_S^{(2)} & \omega G_C^{(2)} & -\omega H_C^{(2)} \end{bmatrix} \cdot \begin{Bmatrix} Q_{xx} \\ Q_{xy} \\ B_{xx} \\ B_{xy} \end{Bmatrix} = \frac{12\rho\omega^2}{h^2} \begin{Bmatrix} \int_\Omega w^C w^{*(1)}\,\mathrm{d}S \\ \int_\Omega w^S w^{*(1)}\,\mathrm{d}S \\ \int_\Omega w^C w^{*(2)}\,\mathrm{d}S \\ \int_\Omega w^S w^{*(2)}\,\mathrm{d}S \end{Bmatrix} \tag{31}$$

If the "cosine" and "sine" parts of the actual curvature fields of the plate are measured all over Ω by means of a suitable full-field measurement technique, the 4×4 components of the left-hand side matrix can be evaluated by numerical integration. Since the points where the kinematics fields are known are regularly spaced, the integrals of Eqs. (27) are simply calculated by linear summations of the products of the local values of the actual and virtual fields weighted by the area of the rectangle surrounding each point of Ω. In the same way, if the two parts, $w^C(x,y)$ and $w^S(x,y)$ of the actual deflection field are measured over Ω, then the four components of the right-hand side term of Eq. (31) can be computed. Therefore, if the 4×4 matrix is regular, the four unknown parameters can be extracted by simply solving the linear system. At this point, it must be pointed out that this method leads to a direct resolution of the inverse problem of material parameter identification and it does not require initial values or iteration scheme. In addition, the method does not require excitation force measurements since the inertial excitation acts as a distributed force actuator over Γ and in the same time as a load cell sensor through the measurement of the harmonic response deflection fields.

4. Virtual fields selection

4.1. General considerations

The selection of the virtual fields is a major task of the identification procedure. As previously mentioned these functions must meet at least two criteria:

- They must insure the independence of the four equations so that the 4×4 matrix can be inverted (see Section 3.8).
- They must cancel out the virtual contribution of the junction forces along the Γ boundary (see Section 3.2).

4.2. Special virtual fields

An adaptation of the so-called "Special virtual fields" introduced by Grédiac et al. [49,50] enforces the first criterion. Originally this concept consists in selecting the virtual functions $u^{*(1)}(x,y)$ and $u^{*(2)}(x,y)$ so that the 4×4 matrix becomes the unity matrix. In the present case, after inverting the order of the second and third lines of the matrix of the linear system equation (31), the functions $u^{*(1)}(x,y)$ and $u^{*(2)}(x,y)$ are selected so that they verify the relations:

- $G_C^{(1)} = 1$ and $G_S^{(1)} = H_C^{(1)} = H_S^{(1)} = 0$;
- $H_C^{(2)} = 1$ and $G_C^{(2)} = G_S^{(2)} = H_S^{(2)} = 0$.

Then the linear system equation (31) becomes

$$\begin{bmatrix} 1 & 0 & 0 & 0 \\ 0 & 1 & 0 & 0 \\ 0 & 0 & \omega & 0 \\ 0 & 0 & 0 & -\omega \end{bmatrix} \cdot \begin{Bmatrix} Q_{xx} \\ Q_{xy} \\ B_{xx} \\ B_{xy} \end{Bmatrix} = \frac{12\rho\omega^2}{h^2} \begin{Bmatrix} \int_\Omega w^C w^{*(1)}\,\mathrm{d}S \\ \int_\Omega w^C w^{*(2)}\,\mathrm{d}S \\ \int_\Omega w^S w^{*(1)}\,\mathrm{d}S \\ \int_\Omega w^S w^{*(2)}\,\mathrm{d}S \end{Bmatrix} \tag{32}$$

Therefore the resolution of the system simply gives

$$Q_{xx} = \frac{12\rho\omega^2}{h^2} \int_\Omega w^C w^{*(1)}\,\mathrm{d}S, \quad B_{xx} = \frac{12\rho\omega}{h^2} \int_\Omega w^S w^{*(1)}\,\mathrm{d}S$$

$$Q_{xy} = \frac{12\rho\omega^2}{h^2} \int_\Omega w^C w^{*(2)}\,\mathrm{d}S, \quad B_{xy} = -\frac{12\rho\omega}{h^2} \int_\Omega w^S w^{*(2)}\,\mathrm{d}S \tag{33}$$

One can remark that this particular adaption of the work by Grédiac is needed regarding the structure of the 4×4 matrix of system equation (31). Simply forcing the latter to be unity leads to incompatible constraints such (e.g.): $G_C^{(1)} = 1$ on the first line and $\omega G_C^{(1)} = 0$ on the second line, etc.

4.3. Virtual field parameterization

As previously mentioned in Section 3.2 the selected virtual fields $u^*(x,y)$ must cancel out the virtual contribution of the connection forces along the Γ boundary which can be written in the present bending case:

$$\int_\Gamma \mathbf{F}\cdot\mathbf{u}^*\,\mathrm{d}S = \int_\Gamma \langle u^* v^* w^* \rangle \begin{Bmatrix} T_x \\ T_y \\ T_z \end{Bmatrix} \mathrm{d}S + \int_\Gamma \langle \theta_x^* \theta_y^* \rangle \begin{Bmatrix} M_x \\ M_y \end{Bmatrix} \mathrm{d}S \tag{34}$$

where the T vector contains the membrane forces (here, only T_z will be nonzero) and the M vector the bending moments. According to Section 3.4 the cancelation of the integral above leads to $w^*(x,y)$, $\theta_x^*(x,y)$ and $\theta_y^*(x,y)$ to be selected as null along the Γ boundary. It is now necessary to examine the expansion of the virtual fields to express these two conditions.

4.3.1. Parameterization 1—polynomial virtual fields

In an earlier study [40] virtual deflection fields such as $w^{*(1)}(x,y) = x^2$ and $w^{*(2)}(x,y) = y^2$ were intuitively chosen. They correctly matched the preceding criteria for a rectangular thin plate theoretically clamped only at one point corresponding to the origin of the coordinates ($x = 0, y = 0$). In this theoretical case the Γ boundary only consists in this point and the virtual fields match the criterion above. As recalled in a section below, the results of simulated identifications carried out using data provided by a corresponding FE model have proved that the principle of this identification procedure is working well. Obviously, such intuitive selection will fail to provide virtual fields matching the preceding criterion along more realistic Γ shapes.

This is the reason why an other parameterization was chosen here.

4.3.2. Parameterization 2—piecewise virtual fields

The main idea of this parameterization [51] consists in meshing the surface of the plate with sub-domains which are chosen rectangular in the present case. These virtual elements are connected through their nodes and the virtual fields on each sub-domain are built up with the degrees of freedom of the nodes of the element using shape functions similar to the ones developed in the finite element method. As mentioned in Section 3.4, the virtual deflection must be C^1 all over Ω. Syed-Muhammad et al. [52] have used the VFM with this parameterization for the material parameter identification of thin plates in static bending. Hermite shape functions [53,54] were used on rectangular virtual elements having four nodes with four degrees of freedom each, namely

$$w^*, \quad \theta_x^* = \frac{\partial w^*}{\partial x}, \quad \theta_y^* = \frac{\partial w^*}{\partial y}, \quad \theta^* = \frac{\partial^2 w^*}{\partial x \partial y} \tag{35}$$

The fourth degree of freedom $\theta_{xy}^*(x,y)$ is necessary to insure the continuity of the virtual slope fields $\theta_x^*(x,y)$ and $\theta_y^*(x,y)$ over the plate.

Then the virtual function $w^*(x,y)$ at any point (x,y) of the virtual sub-domain can be written as

$$w^*(x,y) = \langle \mathbf{g}(x,y) \rangle \{\mathbf{Y}_e^*\} \tag{36}$$

where the row vector $\langle \mathbf{g}(x,y) \rangle$ contains the 16 Hermite shape functions and $\{\mathbf{Y}_e^*\}$ is the 16 components vector of the degrees of freedom of the four nodes of the virtual element, which can be arranged in transposed form:

$${}^{\mathrm{T}}\{\mathbf{Y}_e^*\} = \langle w_{(n1)}^*, \theta_{x(n1)}^*, \theta_{y(n1)}^*, \theta_{xy(n1)}^*, w_{(n2)}^*, \ldots, w_{(n4)}^*, \ldots, \theta_{xy(n4)}^* \rangle \tag{37}$$

where $n1$, $n2$, $n3$, $n4$ are the numbers of the four nodes of the virtual element. The related virtual second derivative fields are therefore parameterized as

$$\kappa_x^*(x,y) = -\frac{\partial^2 \langle \mathbf{g}(x,y) \rangle}{\partial x^2}\{\mathbf{Y}_e^*\}$$

$$\kappa_y^*(x,y) = -\frac{\partial^2 \langle \mathbf{g}(x,y) \rangle}{\partial y^2}\{\mathbf{Y}_e^*\}$$

$$\kappa_s^*(x,y) = -2\frac{\partial^2 \langle \mathbf{g}(x,y) \rangle}{\partial x\,\partial y}\{\mathbf{Y}_e^*\} \tag{38}$$

Obviously, the cancelation of the $w^*(x,y), \theta_x^*(x,y)$ and $\theta_y^*(x,y)$ virtual fields along the Γ boundary is simply reached by forcing the four virtual degrees of freedom of all the nodes belonging to the Γ boundary to be null.

4.3.3. Use of the piecewise virtual fields

In the general case, Ω is meshed using N_e virtual elements globally involving n nodes and finally $N = n \times 4$ virtual degrees of freedom which can be ordered in a vector $\{\mathbf{Y}^*\}$.

On each element denoted e, computation of the four quantities defined in Eq. (28) can be done by replacing the virtual curvatures by their expressions issued from Eq. (38) and using numerical integration on the surface of the element. One can remark that the vector $\{Y_e^*\}$ can be factorized outside the integrals and this leads to

$$G_e^C = \langle \mathbf{GC}_e \rangle \{\mathbf{Y}_e^*\}, \quad G_e^S = \langle \mathbf{GS}_e \rangle \{\mathbf{Y}_e^*\}$$

$$H_e^C = \langle \mathbf{HC}_e \rangle \{\mathbf{Y}_e^*\}, \quad H_e^S = \langle \mathbf{HS}_e \rangle \{\mathbf{Y}_e^*\} \tag{39}$$

where $\langle \mathbf{GC}_e \rangle$, $\langle \mathbf{GS}_e \rangle$, $\langle \mathbf{HC}_e \rangle$ and $\langle \mathbf{HS}_e \rangle$ are row vectors of 16 numerical components each arising from integration over the considered e element.

Using an assembling procedure similar to that of the finite element method, the G and H factors can be calculated over the Ω area relatively to the N virtual DOFs vector $\{\mathbf{Y}^*\}$:

$$G^C = \langle \mathbf{GC} \rangle \{\mathbf{Y}^*\}, \quad G^S = \langle \mathbf{GS} \rangle \{\mathbf{Y}^*\}$$

$$H^C = \langle \mathbf{HC} \rangle \{\mathbf{Y}^*\}, \quad H^S = \langle \mathbf{HS} \rangle \{\mathbf{Y}^*\} \tag{40}$$

In an analogous way, the evaluation of the right hand-side term of Eq. (32) is done by numerical integration on each element after replacing the virtual deflection field by its corresponding expression issued from Eq. (36). The same assembling procedure leads to the expression of the right-hand-side term computed over Ω relatively to the $\{\mathbf{Y}^*\}$ vector:

$$\frac{12\rho\omega^2}{h^2} \int_\Omega w^C w^* \, \mathrm{d}S = \langle \mathbf{RC} \rangle \{\mathbf{Y}^*\}$$

$$\frac{12\rho\omega^2}{h^2} \int_\Omega w^S w^* \, \mathrm{d}S = \langle \mathbf{RS} \rangle \{\mathbf{Y}^*\} \tag{41}$$

As the shape function is issued from the choice of the virtual element type, the selection of the two virtual fields required for the identification equation (31) consists in the selection of two virtual DOF vectors $\{\mathbf{Y}^{*(1)}\}$ and $\{\mathbf{Y}^{*(2)}\}$ which give the identification system:

$$\begin{bmatrix} \langle \mathbf{GC} \rangle \{\mathbf{Y}^{*(1)}\} & \langle \mathbf{HC} \rangle \{\mathbf{Y}^{*(1)}\} & \omega \langle \mathbf{GS} \rangle \{\mathbf{Y}^{*(1)}\} & \omega \langle \mathbf{HS} \rangle \{\mathbf{Y}^{*(1)}\} \\ \langle \mathbf{GS} \rangle \{\mathbf{Y}^{*(1)}\} & \langle \mathbf{HS} \rangle \{\mathbf{Y}^{*(1)}\} & \omega \langle \mathbf{GC} \rangle \{\mathbf{Y}^{*(1)}\} & -\omega \langle \mathbf{HC} \rangle \{\mathbf{Y}^{*(1)}\} \\ \langle \mathbf{GC} \rangle \{\mathbf{Y}^{*(2)}\} & \langle \mathbf{HC} \rangle \{\mathbf{Y}^{*(2)}\} & \omega \langle \mathbf{GS} \rangle \{\mathbf{Y}^{*(2)}\} & \omega \langle \mathbf{HS} \rangle \{\mathbf{Y}^{*(2)}\} \\ \langle \mathbf{GS} \rangle \{\mathbf{Y}^{*(2)}\} & \langle \mathbf{HS} \rangle \{\mathbf{Y}^{*(2)}\} & \omega \langle \mathbf{GC} \rangle \{\mathbf{Y}^{*(2)}\} & -\omega \langle \mathbf{HC} \rangle \{\mathbf{Y}^{*(2)}\} \end{bmatrix} \begin{Bmatrix} Q_{xx} \\ Q_{xy} \\ B_{xx} \\ B_{xy} \end{Bmatrix} = \begin{Bmatrix} \langle \mathbf{RC} \rangle \{\mathbf{Y}^{*(1)}\} \\ \langle \mathbf{RS} \rangle \{\mathbf{Y}^{*(1)}\} \\ \langle \mathbf{RC} \rangle \{\mathbf{Y}^{*(2)}\} \\ \langle \mathbf{RS} \rangle \{\mathbf{Y}^{*(2)}\} \end{Bmatrix} \tag{42}$$

4.4. Piecewise virtual fields selection

4.4.1. Piecewise virtual fields independence

As mentioned at the beginning of Section 4 the selected virtual fields must comply to at least two conditions. Firstly they must be linearly independent to insure the resolution of the linear system equation (42). With the used parameterization, the conditions issued in Section 4.2 become in matrix form:

$$\begin{bmatrix} \langle \mathbf{GC} \rangle \\ \langle \mathbf{GS} \rangle \\ \langle \mathbf{HC} \rangle \\ \langle \mathbf{HS} \rangle \end{bmatrix} [\{\mathbf{Y}^{*(1)}\} \ \ \mathbf{Y}^{*(2)}\}] = \begin{bmatrix} 1 & 0 \\ 0 & 0 \\ 0 & 1 \\ 0 & 0 \end{bmatrix} \tag{43}$$

4.4.2. Cancelation of the virtual contribution of the junction force

The cancelation of the virtual contribution of the junction forces along the Γ boundary implies the nullity of the virtual deflection fields and virtual slope fields along this boundary. That is achieved by zeroing the four virtual degrees of freedom of each of the n_Γ nodes belonging to the boundary. The matrix form of these $n_\Gamma \times 4 \times 2$ conditions can be written as

$$[\mathbf{F}][\{\mathbf{Y}^{*(1)}\} \ \ \{\mathbf{Y}^{*(2)}\}] = \begin{bmatrix} 0 & 0 \\ \vdots & \vdots \\ 0 & 0 \end{bmatrix} \tag{44}$$

where $[\mathbf{F}]$ is the localization matrix of the conditions with $n_\Gamma \times 4$ lines and N columns.

An infinity of piecewise virtual fields defined by virtual degree of freedom vectors $\{\mathbf{Y}^{*(\alpha)}\}(\alpha = 1, 2)$ can match the two preceding constraints 4.4.1 and 4.4.2. The final selection of optimized virtual fields is carried out through the choice of virtual DOF vectors $\{\mathbf{Y}^{*(\alpha)}\}$ which minimize the effect of the measurement noise on the identified parameters.

4.4.3. Final selection by minimization of the effect of noisy data

This minimization was developed by Avril [42] and originally applied to the virtual fields selection for elastic parameters identification in the case of in-plane deformations of a plate specimen. It is based on the reasonable hypothesis of a Gaussian nature of the noise which is added to the curvature field measurements. This work has shown that the standard deviation of the identified parameters is proportional to the standard deviation γ of the added noise. This proportionality can be written as

$$Std(Q_{ij}, B_{ij}) = \gamma \eta^{(\alpha)} \tag{45}$$

where $\eta^{(\alpha)}$ can be seen as the sensitivity of the identification procedure to the noise. Its minimization can be used as final criterion for the virtual fields selection. The objective function used for that purpose has been defined [42] by

$$(\eta^{(\alpha)})^2 = 1/2 \langle \mathbf{Y}^{*(\alpha)} \rangle [\mathbf{P}] \{\mathbf{Y}^{*(\alpha)}\} \quad (\alpha = 1,2) \tag{46}$$

where **P** is a semi-definite matrix depending on the unknown material parameters. It is an adaptation to the present case of the study reported in [52]. Since the optimized $\{Y^{*(\alpha)}\}$ must verify the above conditions 4.4.1 and 4.4.2, the minimization has to be performed with constraints. The latter are simply written by bringing together Eqs. (43) and (44):

$$[\mathbf{A}]\{\mathbf{Y}^{*(\alpha)}\} = \{\mathbf{Z}^{(\alpha)}\} \quad (\alpha = 1,2) \tag{47}$$

where [*A*] is the localization matrix of the constraints simply obtained by joining the two left hand-side matrices of equations (43) and (44) while $\{\mathbf{Z}^{(\alpha)}\}$ represents the two vectors of constraints resulting from the junction of the two right hand-side terms of the same equations.

Therefore, the Lagrangian of the minimization can be written as

$$\mathcal{L}^{\alpha} = 1/2 \langle \mathbf{Y}^{*\alpha} \rangle [\mathbf{P}] \{\mathbf{Y}^{*\alpha}\} + \langle \mathbf{\Lambda}^{\alpha} \rangle ([\mathbf{A}]\{\mathbf{Y}^{*\alpha}\} - \{\mathbf{Z}^{\alpha}\}) \quad (\alpha = 1,2) \tag{48}$$

where $\langle \mathbf{\Lambda}^{\alpha} \rangle$ denotes the row vector of the Lagrangian multiplicators. The optimized virtual vectors $\{\mathbf{Y}^{*(\alpha)}\}$ are obtained by solving the associated linear system:

$$\left[\begin{array}{c|c} \mathbf{P} & {}^{T}\mathbf{A} \\ \hline \mathbf{A} & \mathbf{0} \end{array}\right] \left\{\begin{array}{c} \mathbf{Y}^{*(\alpha)} \\ \hline \mathbf{\Lambda}^{(\alpha)} \end{array}\right\} = \left\{\begin{array}{c} \mathbf{0} \\ \hline \mathbf{Z}^{(\alpha)} \end{array}\right\} \qquad (\alpha = 1,2) \tag{49}$$

where ${}^{T}\mathbf{A}$ denotes the transpose of the matrix *A*. Since **P** depends on the unknown parameters, an iterative algorithm is used with a convergence criterion based upon the relative difference between two consecutive results [42]. Tests have shown that the convergence is quickly reached after two or three iterations.

The obtained optimized virtual vectors $\{\mathbf{Y}^{*(\alpha)}\}$ describe the virtual fields which comply with the two necessary criteria and are the less sensitive to the measurement noise. They lead to the maximum likelihood solution.

5. Identification on simulated data

5.1. Considered case

The considered coupon of the isotropic tested material is a rectangular thin plate which is free on its external boundary. This plate is clamped in its centre over a small area Π to an excitation device which imposes a sine driving movement in the out-of-plane direction. In that case, Γ is a closed line surrounding the clamped area. It splits the plate in two zones: the internal one, Σ, which contains the clamping and the rest of the plate, Ω, which external boundary remains free (see Fig. 2).

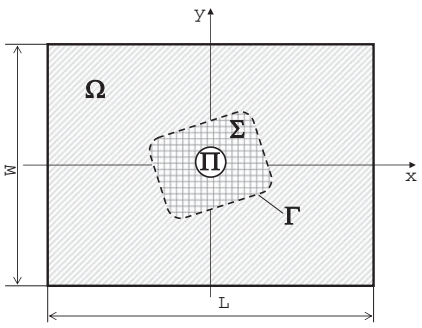

Fig. 2. Considered plate.

5.2. Finite element model

In order to simulate the identification on the considered case, a finite element model has been built up using 100×80 shell elements from a standard FE code. The parameters of this model are shown in Table 1 where ϕ is the diameter of the circular area Π and β the proportional damping factor introduced in the model such that

$$\beta = \frac{B_{xx}}{Q_{xx}} = \frac{B_{xy}}{Q_{xy}} \tag{50}$$

The stiffness and damping values introduced in the FE model are very close to the ones obtained from previous tests on the same material used in tests below (see Section 6). Harmonic vibrating responses of this plate model have been computed and used as entry data to the identification procedure. In order to check the effects of the measurement noise on the identification results, random perturbations are added, in certain cases, to the computed deflection and curvature fields. The chosen standard deviation of this added noise is $\gamma = 10^{-3}\,\mathrm{m}^{-1}$, which is realistic with regards to the actual measurement noise. Relative errors between the reference and identified parameters have been monitored and results are reported in the following.

5.3. Simulated identifications with polynomial virtual fields

Table 2 shows results similar to that presented in [40] where intuitively chosen virtual deflection fields ($w^{*(1)}(x,y) = x^2$ and $w^{*(2)}(x,y) = y^2$) were used for identification on simulated data, without noise, provided by the FE model of the same plate but only clamped at one point ($\phi = 0$). The vibrating responses of the plate to harmonic inertial excitation at five frequencies were used. It must be pointed out that the 100 Hz excitation frequency is very close to a resonance of the plate, the four others corresponding to nonresonant situations.

Since the virtual fields and their first derivatives are null at the clamped point ($x = 0, y = 0$), they match the second criterion and the identification results are correct.

The same virtual fields have been applied to simulated data provided by the FE model presented in Section 5.2 without noise addition. The results presented in Table 3 do not reach the same quality. Obviously these virtual fields do not cancel the second integral along the Γ border and its contribution disturbs the identification procedure (see Eq. (7)).

In order to improve this result by using intuitively defined virtual fields, the following can be used: $w^{*(1)} = x^4$ and $w^{*(2)} = y^4$. Zeroing higher order derivatives at the clamp point will reduce the bias coming from the virtual contribution of the clamping forces, as can be seen in Table 4. Unfortunately, because of the higher degree of the polynomials these results tend to be very sensitive to noise in the data as shown in Table 5 where each mean result is the average of eight simulated identifications.

Another possibility of automatic generation of virtual deflection fields on a polynomial basis inspired by [50], was undertaken using an algorithm described by the following equations:

$$w^*(x,y) = \begin{cases} \displaystyle\sum_{k=0}^{n} \sum_{\substack{j=0 \\ (i=k-j)}}^{k} A_{ij}(x^2+y^2-r^2)^2 \left(\frac{x}{a}\right)^i \left(\frac{y}{b}\right)^j, & (x^2+y^2 > r^2) \\ 0, & (x^2+y^2 \le r^2) \end{cases} \tag{51}$$

where A_{ij} are the coefficients of the monomials $x^i y^j$ and $r \ge \phi/2$ is the radius of the circle defining the Γ closed line. Since this type of virtual fields strictly matches the second condition, the identification results using data without noise are quite satisfactory. But even for low degrees of the polynomials ($n = 3$ or 4 e.g.), the robustness to noise is rather poor as shown in Table 6.

One way to solve this issue properly is to switch to piecewise virtual fields where the conditions to be respected along the Γ boundary can be exactly enforced and noise optimization can be carried out.

Table 1
Geometrical parameters, material characteristics and normalized parameters of the FE model.

L (mm)	W (mm)	h (mm)	ϕ (mm)	ρ (kg m^{-3})	E (GPa)	ν	β (s)	Q_{xx} (GPa)	Q_{xy} (GPa)	B_{xx} (10^5 Pa s)	B_{xy} (10^5 Pa s)
200	160	3	18	1190	5	0.3	10^{-4}	5.494	1.648	5.494	1.648

Table 2
Identification relative errors, point clamped plate, $w^{*(1)} = x^2$ and $w^{*(2)} = y^2$, exact data.

Freq. (Hz)	70	80	90	100	110
Rel. err Q_{xx} (%)	−0.01	−0.04	−0.02	−0.05	−0.4
Rel. err Q_{xy} (%)	−0.02	−0.05	0.01	−0.01	−0.1
Rel. err B_{xx} (%)	−0.01	−0.02	−0.00	−0.02	−0.6
Rel. err B_{xx} (%)	−0.02	−0.14	−0.16	−0.25	−0.7

Table 3
Identification relative errors, area clamped plate, $w^{*(1)}=x^2$ and $w^{*(2)}=y^2$, exact data.

Freq. (Hz)	70	80	90	100	110
Rel. err Q_{xx} (%)	6.9	6.7	6.4	6.2	6.0
Rel. err Q_{xy} (%)	6.0	5.5	5.2	5.1	4.9
Rel. err B_{xx} (%)	7.0	12.3	7.9	8.2	8.0
Rel. err B_{xy} (%)	7.6	15.2	8.1	12.1	9.1

Table 4
Identification relative errors, area clamped plate, $w^{*(1)}=x^4$ and $w^{*(2)}=y^4$, exact data.

Freq. (Hz)	70	80	90	100	110
Rel. err Q_{xx} (%)	0.02	0.02	0.01	0.00	0.00
Rel. err Q_{xy} (%)	0.04	0.03	0.02	0.01	0.01
Rel. err B_{xx} (%)	0.04	0.12	0.05	0.05	0.05
Rel. err B_{xy} (%)	0.06	0.22	0.08	0.10	0.07

Table 5
Identification relative errors, area clamped plate, $w^{*(1)}=x^4$ and $w^{*(2)}=y^4$, noisy data.

Freq. (Hz)	70	80	90	100	110
Rel. err Q_{xx} (%)	−0.13	−0.01	0.01	0.01	−0.01
Rel. err Q_{xy} (%)	0.15	0.11	0.03	0.03	−0.01
Rel. err B_{xx} (%)	0.55	1.57	−0.30	−0.13	0.08
Rel. err B_{xy} (%)	6.79	−0.76	0.77	0.28	0.09

Table 6
Identification relative errors, area clamped plate, polynomial virtual fields $n=3$, noisy data.

Freq. (Hz)	70	80	90	100	110
Rel. err Q_{xx} (%)	0.26	−0.01	0.01	−0.01	−0.01
Rel. err Q_{xy} (%)	−0.34	−0.20	0.10	0.10	0.11
Rel. err B_{xx} (%)	−3.30	−1.08	0.28	0.05	0.02
Rel. err B_{xy} (%)	8.37	0.89	0.53	0.16	0.40

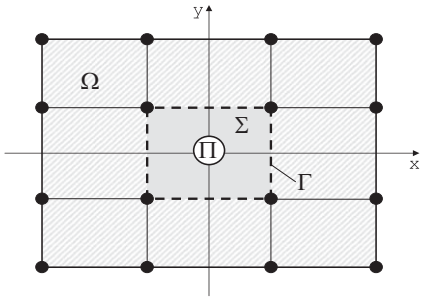

Fig. 3. Meshed plate.

5.4. Simulated identification with piecewise virtual fields

The chosen fictitious Γ boundary was selected as a rectangle surrounding the clamping area. The reason for extending the excluded area a bit further from the actual clamping zone was that measurements around the bolt were generally of poorer quality than that further away from stress concentrations. A 3×3 mesh of 9 rectangular elements was defined on the surface of the plate thanks to $n=16$ nodes (see Fig. 3) such that the external boundary of the central element (in grey on the figure) corresponds to the Γ line. Therefore, the definition of a piecewise virtual field over Ω uses the $N_e=8$ peripheral elements involving $N=16\times4$ ($n\times4$) virtual degrees of freedom. In this particular case, the enforcement of the

second criterion is simply obtained by zeroing the four degrees of freedom of each node defining the central virtual element. The identification results are reported in Table 7 for exact FE data.

Identifications have been carried out using simulated data with addition of random noise on the curvature fields with the same standard deviation $\gamma = 10^{-3}\,\mathrm{m}^{-1}$ as mentioned in Section 5.2. Table 8 presents the mean relative errors on the averaged results of eight identifications. For each of these latter, final selection of piecewise virtual fields has been achieved using the procedure for minimizing the effect of the measurement noise presented in Section 4.4.3. Other simulations of identification have been performed with the same noisy data and using 5×5 piecewise virtual fields. The results were quite similar. Therefore, 3×3 piecewise virtual fields have been retained for processing the following experimental data.

6. Experimental results

6.1. Introduction

Experiments with the same geometry and loading as that of the previous FE model have been performed on polycarbonate plates. To obtain a reference, elastic and damping material parameters, Young modulus E and loss factor $\eta = \tan(\delta)$, have been identified from classical tests performed by the authors on vibrating beams in the same frequency range and confirmed by tests using dynamic mechanical thermal analysis (DMTA) concerning the loss factor. The reference for Poisson's ratio v was taken from the literature [55,56]. These reference values are shown in Table 9.

Full-field measurements have been carried out using the experimental arrangement and procedure completely presented in [41]. The principal points are recalled below. A driving device associated with an electrodynamic shaker imposes a bending inertial excitation to the tested plate (see Fig. 4). Since deflection and curvature fields are needed for the identification, the measurement of the slope fields was preferred to avoid noise problems arising from double differentiation of the measured deflection field. The measurements of these fields were achieved using deflectometry which is a noninterferometric technique in white light [19,57]. A cross line grating (grid) is placed in front of the tested plate which must have a mirror like reflective surface. The image of the grid on the surface of the plate is observed with a CCD camera. When the plate bends, the image of the grid seen by the camera changes too. At first an image is taken at rest, and a second on the deformed plate. The reference grid serves as a ruler and its images are analysed using spatial phase-stepping which enables a refined evaluation of the spatial phase of the subtracted images [58]. As previously shown in Section 3, the identification procedure requires the fields taken at two instants just separated by a quarter of period of the driving movement. This is achieved by freezing the images of the grid by the use of an electronic flash device accurately triggered by the signal provided by an accelerometer fixed on the driving bar (see Fig. 4).

An example of measured absolute deflection fields are shown in Fig. 5. It concerns the vibrating response of the original plate which is excited at 100 Hz, very close to a resonance, by a 16 μm amplitude driving movement. For the sake of legibility of the figures, no scale bars are drawn for the responses. Cosine and sine parts are drawn with the same gray scale. The black and white colours refer to the extreme absolute deflections and the corresponding values are indicated. On each window the black circle mark locates the clamping point.

6.2. Experimental result presentation

For comparison with the reference values, the results of the following identifications are presented under the form of engineering elastic constants and loss factors which have been extracted from the identified complex stiffness components as [59]

$$\hat{Q}_{xx} = Q_{xx} + \mathrm{j}\omega B_{xx}$$

$$\hat{Q}_{xy} = Q_{xy} + \mathrm{j}\omega B_{xy} \tag{52}$$

Then, complex Young's modulus $\hat{E}$ and Poisson's ratio $\hat{v}$ are calculated as

$$\hat{v} = \frac{\hat{Q}_{xx}}{\hat{Q}_{xy}}, \quad \hat{E} = \hat{Q}_{xx}\,(1-\hat{v}^2) \tag{53}$$

Table 7
Identification relative errors, area clamped plate, 3×3 piecewise virtual fields, exact data.

Freq. (Hz)	70	80	90	100	110
Rel. err Q_{xx} (%)	0.05	0.04	0.03	0.01	0.01
Rel. err Q_{xy} (%)	−0.09	−0.15	−0.09	−0.08	−0.07
Rel. err B_{xx} (%)	0.05	0.05	0.04	0.01	0.01
Rel. err B_{xy} (%)	−0.11	−0.19	−0.11	−0.10	−0.09

Table 8
Identification relative errors, area clamped plate, 3×3 piecewise virtual fields, noisy data.

Freq. (Hz)	70	80	90	100	110
Rel. err Q_{xx} (%)	−0.29	0.03	−0.03	0.02	−0.11
Rel. err Q_{xy} (%)	−0.49	−0.29	−0.16	−0.14	−0.24
Rel. err B_{xx} (%)	1.28	−0.26	1.06	−0.04	−0.37
Rel. err B_{xy} (%)	1.58	−1.49	1.56	−0.27	−0.60

Table 9
Geometrical parameters and material characteristics of the tested plate.

L (mm)	W (mm)	h (mm)	ϕ (mm)	ρ (kg m^{-3})	E (GPa)	v	$\eta = \tan(\delta)$
200	160	3	18	1190	4.90	0.3	0.056

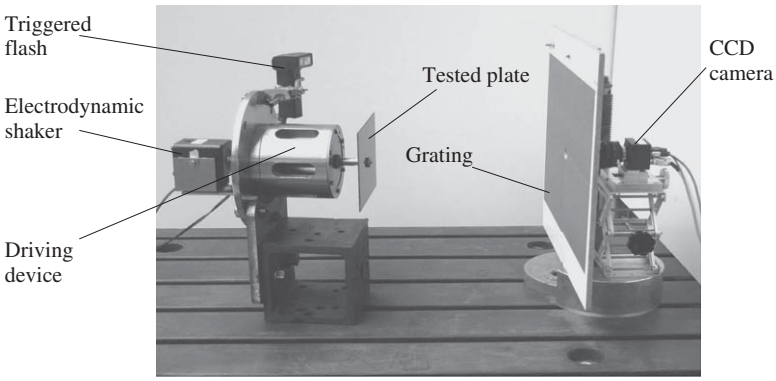

Fig. 4. View of the experimental arrangement.

that leads to the elastic engineering constants:

$$E = \mathrm{Re}(\hat{E}), \quad v = \mathrm{Re}(\hat{v}) \tag{54}$$

and to the loss factor $\tan(\delta)$ and Poisson's ratio loss factor η_v:

$$\tan(\delta) = \frac{\mathrm{Im}(\hat{E})}{\mathrm{Re}(\hat{E})}, \quad \eta_v = -\frac{\mathrm{Im}(\hat{v})}{\mathrm{Re}(\hat{v})} \tag{55}$$

For each parameters, the mean value is computed from identifications provided by several measurements performed at the same excitation frequency. Coefficients of variation are also calculated by normalizing the standard deviations with the corresponding mean value and presented in percentage.

6.3. Previous identifications

Table 10 recalls the results previously presented in [41] and recalculated with the procedure above. These first results have been obtained from four measurements at each frequency and processed with intuitively selected virtual fields $w^{*(1)} = x^2$ and $w^{*(2)} = y^2$ which did not match the second criterion since the coupon was clamped at the end of the driving bar through a 18 mm diameter circular area. The results were not so bad except for Poisson's ratio loss factor.

6.4. Identification with optimized virtual fields

Table 11 presents the identification results achieved with optimized piecewise virtual fields. The mean values and the coefficients of variation come from eight full-field measurements at each frequency. It can be seen that the results are similar to that obtained with the x^2 and y^2 virtual fields but this time, the results for Poisson's ratio loss factor are much more stable, which confirms the interest of using such optimized virtual fields.

One of the advantages of the present procedure is that the identified parameters are independent from anything that happens outside the considered subpart of the plate. This is extremely important since one of the major problems in material damping identification is to separate the damping coming from the specimen from that coming to its connection

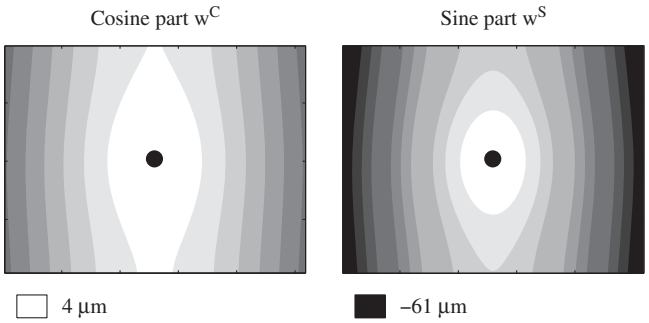

Fig. 5. Measured absolute deflection fields at 100 Hz on the original plate.

Table 10
Experimentally identified engineering constants and loss factors $w^{*(1)}=x^2$ and $w^{*(2)}=y^2$.

Frequency (Hz)	70	80	90	100	110
E (GPa)					
Mean	4.79	4.69	4.71	4.71	4.72
Coeff. var. (%)	2.8	1.1	1.1	1.2	1.4
v					
Mean	0.32	0.31	0.30	0.30	0.31
Coeff. var. (%)	2.4	1.9	1.9	1.9	2.1
$\tan(\delta)$					
Mean	0.054	0.055	0.062	0.069	0.067
Coeff. var. (%)	3.6	2.3	2.6	2.9	2.9
η_v					
Mean	0.0040	0.0015	0.022	0.0063	0.041
Coeff. var. (%)	–	–	10.7	12.3	11.8

Table 11
Experimentally identified engineering constants and loss factors with optimized piecewise virtual fields.

Frequency (Hz)	70	80	90	100	110
E (GPa)					
Mean	4.62	4.63	4.70	4.55	4.69
Coeff. var. (%)	1.8	1.3	1.2	0.8	0.6
v					
Mean	0.33	0.33	0.3	0.34	0.34
Coeff. Var. (%)	1.3	0.5	0.8	0.6	0.6
$\tan(\delta)$					
Mean	0.065	0.052	0.050	0.064	0.062
Coeff. var. (%)	2.9	1.8	1.8	1.9	1.1
η_v					
Mean.	0.024	0.013	0.014	0.031	0.022
Coeff. var. (%)	10.3	4.7	6.0	9.1	7.1

to the excitation set up (boundary conditions). To illustrate this very nice feature, two showcases are given thereafter, both with some additional damping added either with a viscoelastic layer bonded on some part of the plate or with rubber bushes added at the clamp.

6.5. Influence of the test configuration and boundary conditions

If the selected virtual fields effectively cancel out the virtual contributions of the junction forces along the Γ border, the procedure only takes into account the mechanical phenomena over the Ω area of interest. Theoretically the effects of the mechanical phenomena outside Ω vanish and in particular the effects of the boundary conditions imposed by the experimental fixture. The two particular tests presented below intend to prove that the proposed procedure can greatly minimize the parasitic effects of the boundary conditions.

6.5.1. Test with a viscoelastic layer

In this test, a patch of viscoelastic material was bonded on the back face of the preceding plate (see Fig. 6). The mass per surface unit of this material is approximatively the same as that of the polycarbonate plate. Due to the heavy damping of the patch material and its added mass, the vibrating behaviour of the tested plate drastically changes. Fig. 7 shows the absolute measured deflection fields in such conditions with an excitation at 100 Hz. To allow the comparison with the responses presented in Fig. 5 the minimum and maximum values are normalized to the same driving amplitude of 16 μm. Due to the patch bonded on the right hand-side of the clamp, the fields present no more symmetry unlike the original case and the amplitudes are reduced. The dimensions and the position of the patch are such that the latter is completely contained in the uniform grey Σ area shown in Fig. 8. Obviously, the Ω area of interest is now the slightly hatched part of the plate shown in the same figure. The same type of optimized 3×3 piecewise virtual fields have been used. The enforcement of the second criterion is simply obtained by zeroing the four virtual degrees of freedom of each of the six nodes defining the Γ border between Σ and Ω (dashed line in Fig. 8). Table 12 presents the results of the identifications from measurements at two excitation frequencies: 80 and 100 Hz. Mean values and coefficients of variation have been obtained from four identifications at each frequency. It is very interesting to note that the identified values are very close to that obtained when there was not viscoelastic patch, although the global damping of the plate has increased quite dramatically.

For the sake of comparisons, Table 13 shows the results of identifications issued from the preceding measurements and carried out using different virtual fields, respectively, piecewise optimized 3×3 ones and intuitively chosen $w^{*(1)} = x^2, w^{*(2)} = y^2$ or $w^{*(1)} = x^4, w^{*(2)} = y^4$ virtual fields. Since these latter are defined all over the plate, noticeable differences could be observed between the three sets of identified values for each two excitation frequencies. In particular when using these two virtual fields, the local addition of mass due to the patch cannot be taking in account and the density ρ in the identification equation (31) is underestimated. That leads to the underestimation of the Young modulus E which can be noticed in Table 13. On the other hand, since the two stiffnesses Q_{xx} and Q_{xy} are both affected by these underestimations, the identified Poisson ratios remained correct.

6.5.2. Test with plate clamped between two rubber washers

In the initial test, the plate was clamped between the end of the driving bar and a thick rigid washer of the same diameter. In this demonstrating test two rubber washers, approximatively 1 mm thick and 20 mm external diameter, were inserted between the faces of the initial plate and the clamping surfaces (see Fig. 9). The difference between these two fastenings is clearly visible on the image of Fig. 10. The (a) window shows the image of the grid around the clamping area when the plate is rigidly clamped. Due to the edge effect around the rigid washer, the distortion of the grid image shows the deformation of the plate surface. In window (b), since the tightening force are more smoothly spread thanks to the rubber washers, the grid image shows very few distortion. In spite of the different boundary conditions provided by these two fastenings, the proposed procedure enables to correctly identify the material constants of the plate.

The first accelerometer mounted on the driving bar (see Fig. 9) measures the driven movement provided by the exciting device. The second miniature accelerometer stuck on the back face of the plate as close as possible to the clamped area gives an evaluation of the solid movement of the plate. Due to the dissipation in the rubber washers, the amplitude of the solid movement of the plate is 14 percent less than that of the driving bar and the phase lag between the two is 34°. This shows that considerable structural damping is added with the rubber washers. In the present case, the Ω area of interest consists in the eight external elements shown in Fig. 3. The enforcement of the second criterion is reached by zeroing the degrees of freedom of the nodes defining the central element enclosing the clamping area. Table 14 shows the identification results at 100 Hz. Mean values and coefficients of variation have been obtained from four identifications.

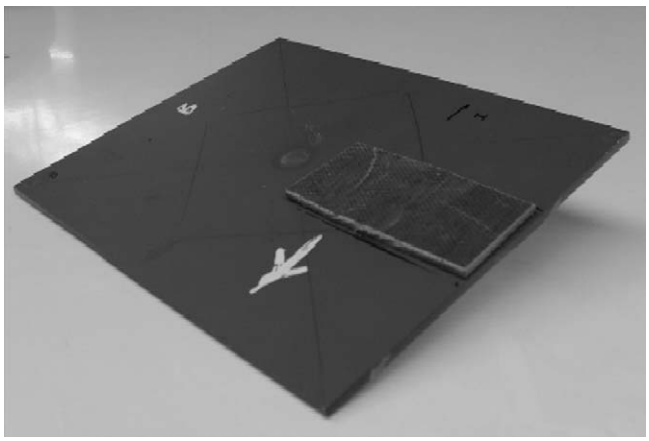

Fig. 6. Plate with viscoelastic patch.

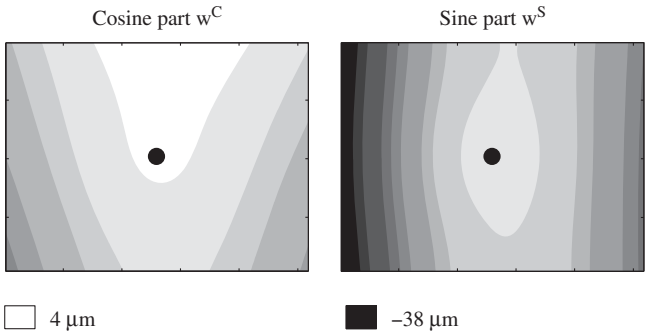

Fig. 7. Measured absolute deflection fields at 100 Hz on the plate with the viscoelastic patch.

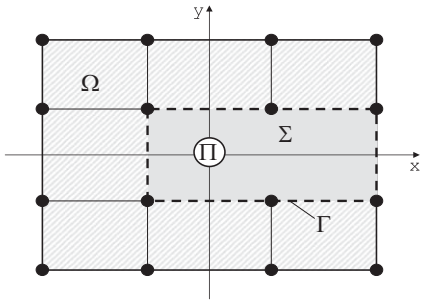

Fig. 8. Meshed plate with viscoelastic patch.

Table 12
Experimental identifications with a viscoelastic patch on the rear face of the plate.

Frequency (Hz)	80 Without visco.	80 With visco.	100 Without visco.	100 With visco.
E (GPa)				
Mean	4.63	4.63	4.55	4.58
Coeff. var. (%)	1.4	1.0	0.8	2.1
v				
Mean	0.33	0.34	0.34	0.34
Coeff. var. (%)	0.5	1.7	0.6	1.2
tan(δ)				
Mean	0.052	0.054	0.064	0.071
Coeff. var. (%)	1.8	9.1	1.9	9.9
η_v				
Mean	0.013	0.070	0.031	0.076
Coeff. var. (%)	4.7	10.3	9.1	16.1

Again, the results are consistent with that obtained on the plate without the rubber washers and on the plate with the viscoelastic patch. The present results clearly demonstrate the power of the identification procedure compared to usual techniques. It should also be pointed out that the damping parameter associated to Poisson's ratio is still not obtained in a very stable manner. This is thought to be cause mainly by issues related to the triggering. It should be possible to get rid of this problem either by improving the triggering or by using a high speed camera to over sample the full-field measurements during a couple of periods of excitation to obtain a nice temporal description of the deformation fields.

7. Conclusion

This papers has shown how full-field measurements applied to a vibrating plate could be used to extract material stiffness and damping parameters without any information about the excitation. The main original idea is to use the inertial forces over the plate to balance out the internal forces (stresses). The inertial forces can, be obtained by double time differentiation of the deflection field and the strains from spatial differentiation of the deformation field. A very important consequence of this approach is that a portion of the tested structure can be isolated and the data processed regardless of

Table 13
Experimental identifications with a viscoelastic patch on the rear face of the plate.

Frequency (Hz)	80			100		
Virtual fields	3×3	x^2, y^2	x^4, y^4	3×3	x^2, y^2	x^4, y^4
E (GPa)						
Mean	4.63	4.38	4.13	4.58	4.38	4.05
Coeff. var. (%)	1.0	3.58	4.01	2.1	2.2	1.6
v						
Mean	0.34	0.37	0.37	0.34	0.35	0.33
Coeff. var. (%)	1.7	1.55	1.7	1.2	1.6	3.0
$\tan(\delta)$						
Mean	0.054	0.064	0.077	0.071	0.070	0.099
Coeff. var. (%)	9.1	9.9	24.3	9.9	12.2	17.5
η_v						
Mean	0.070	0.037	0.046	0.076	0.074	0.090
Coeff. var. (%)	10.3	28	41	16.1	13.4	16.4

Results from different types of virtual fields (3×3 from previous Table 12).

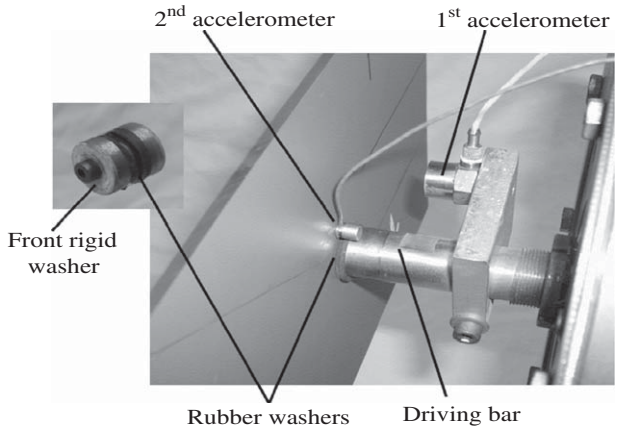

Fig. 9. Plate fastening with rubber washers—fixture details.

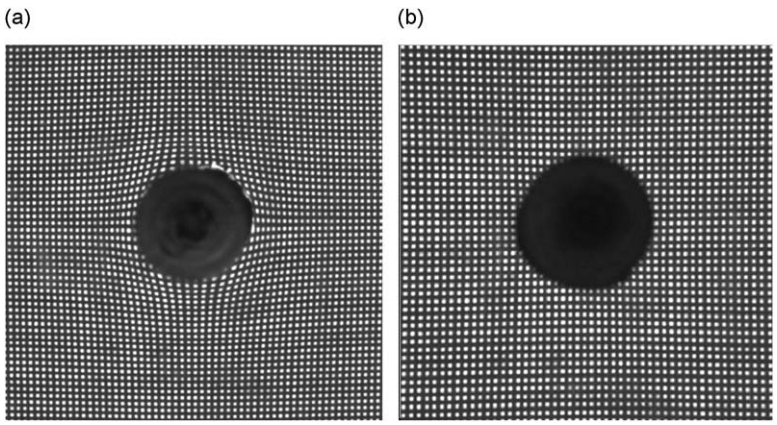

Fig. 10. Grid images around the clamping: (a) without rubber washers; (b) with rubber washers.

what happens in the rest of the structure. To illustrate this, the paper showed a test case on a rectangular polymer plate inertially excited at frequencies around 100 Hz. It was shown that the same material stiffness and damping parameters could be obtained on the standard plate test and on tests where additional damping was introduced at the plate level (with a viscoelastic layer) and at the clamp level (rubber bush). It should also be noted that since a plate is tested, the procedure

Table 14
Experimental identifications with the plate clamped between rubber washers.

Frequency (Hz)	100 Without rubber washers	100 With rubber washers
E (GPa)		
Mean	4.55	4.59
Coeff. var. (%)	0.8	2.1
ν		
Mean	0.34	0.34
Coeff. var. (%)	0.6	2.9
$\tan(\delta)$		
Mean	0.064	0.058
Coeff. var. (%)	1.9	10.9
η_ν		
Mean	0.031	0.016
Coeff. var. (%)	9.1	12.1

gives access to both complex moduli, i.e., also to the damping parameters associated with Poisson's ratio, which usual procedures struggle to measure.

There are still quite a few improvements to be brought to the procedure to make it fully robust. One of the issues concerns the triggering of image freezing. Since damping is basically related to a small time lag between stress and strain, this issue has a direct impact on the quality of the identified values. Tests with a high speed camera are underway to tackle this problem. The second issue is the fact that since only surface measurements are performed, a thin plate assumption has to be made. This might be a problem for thicker plates especially at higher frequencies where deformed shapes will be more complex and local transverse shear effects may become significant. There are some ideas underway to tackle this and as a last resort, finite element model updating may be used. Finally, the full-field measurement technique used in this paper, deflectometry, requires a flat and reflective plate. It is essential to prove that good measurements could also be obtained with deflection measurements (with fringe projection or stereo image correlation) for the method to become more general. This will be attempted in the near future. It should also be noted that even though an isotropic constitutive model is assumed here, the method can be applied to anisotropic materials such as composites. In this case, the selection of the virtual fields will be more critical but the main problem will be that at a single frequency, the experimental data may not contain enough information to identity the whole set of stiffnesses. Combination of several test configurations may then be required, this is presently underway.

Acknowledgements

The authors would like to thank the Champagne-Ardennes Regional Council for the financial support of this study, as well as one of the reviewers for a very extensive and useful review.

References

[1] H. Sol, Identification of Anisotropic Plate Rigidities Using Free Vibration Data, PhD Thesis, Free University of Brussels, 1986.
[2] L.R. Deobald, R.F. Gibson, Determination of elastic constants of orthotropic plates by a modal analysis/Rayleigh–Ritz technique, *Journal of Sound and Vibration* 124 (2) (1988) 269–283.
[3] K.E. Fällström, M.A. Jonsson, A non-destructive method to determine material properties in anisotropic plates, *Polymer Composites* 12 (5) (1991) 293–305.
[4] P. Pedersen, P.S. Frederiksen, Identification of orthotropic materials moduli by combinated experimental numerical approach, *Measurements* 10 (1992) 113–118.
[5] W.P. De Wilde, Identification of the rigidities of composite systems by mixed numerical/experimental methods, in: A. Vautrin, H. Sol (Eds.), *Mechanical Identification of Composites*, Elsevier Science Publishers, 1991, pp. 1–15.
[6] E.O. Ayorinde, R.F. Gibson, Elastic constants of orthotropic composite materials using plate resonance frequencies, classical lamination theory and an optimized three-mode Rayleigh formulation, *Composites Engineering* 3 (5) (1993) 395–407.
[7] C.M. Mota Soares, M. Moreira de Freitas, A.L. Araujo, P. Pedersen, Identification of material properties of composite plate specimen, *Composite Structures* 25 (1993) 277–285.
[8] P. Frederiksen, Identification of elastic constants including transverse shear moduli of thick orthotropic plates, Technical Report, Danish Centre for Applied Mathematics and Mechanics, 1995 (Report number 500).
[9] A.L. Araujo, C.M. Mota Soares, M.J.M. Freitas, Characterization of material parameters of composite specimens using optimization and experimental data, *Composites Part B* 27 (2) (1996) 185–191.
[10] H. Sol, H. Hua, J. De Visscher, J. Vantomme, W.P. De Wilde, A mixed numerical experimental technique for the non destructive identification of the stiffness properties of fibre reinforced composite materials, *NDT&E International* 30 (2) (1997) 85–91.
[11] L. Pagnotta, G. Stigliano, Elastic characterization of isotropic plates of any shape via dynamic tests: theoretical aspects and numerical simulations, *Mechanics Research Communications* 35 (2008) 351–360.
[12] P.S. Frederiksen, Numerical studies for identification of orthotropic elastic constants of thick plates, *European Journal of Mechanics A/Solids* 16 (1997) 117–140.

[13] P.S. Frederiksen, Experimental procedure and results for the identification of elastic constants of thick orthotropic plates, *Journal of Composite Materials* 31 (4) (1997) 360–382.
[14] K.E. Fällström, K. Olofsson, H.O. Saldner, S. Schedin, Dynamic material parameters in an isotropic plate estimated by phase-stepped holographic interferometry, *Optics and Lasers in Engineering* 24 (5–6) (1996) 429–454.
[15] J. Cunha, J. Piranda, Application of model updating techniques in dynamics for the identification of elastic constants of composite materials, *Composites Part B* 30 (1999) 79–85.
[16] J. Cugnoni, T. Gmür, A. Schorderet, Identification by modal analysis of composite structures modelled with FSDT and HSDT laminated shell finite elements, *Composites Part A* 35 (7–8) (2004) 977–987.
[17] M. Grédiac, N. Fournier, P.-A. Paris, Y. Surrel, Direct determination of elastic constants of anisotropic plates by modal analysis: experimental results, *Journal of Sound and Vibration* 210 (5) (1998) 643–659.
[18] M. Grédiac, P.-A. Paris, Direct identification of elastic constants of anisotropic plates by modal analysis: theoretical and numerical aspects, *Journal of Sound and Vibration* 193 (3) (1996) 401–415.
[19] Y. Surrel, N. Fournier, M. Grédiac, P.-A. Paris, Phase-stepped deflectometry applied to shape measurement of bent plates, *Experimental Mechanics* 39 (1) (1999) 66–70.
[20] F.B. Batista, E.L. Albuquerque, J.R.F. Arruda, M. Dias Jr., Identification of the bending stiffness matrix of symmetric laminates using regressive discrete fourier series and finite differences, *Journal of Sound and Vibration* 320 (2009) 793–807.
[21] R.F. Gibson, Modal vibration response measurements for characterization of composite materials and structures, *Composites Science and Technology* 60 (2000) 2769–2780.
[22] G.G. Wren, V.K. Kinra, On the effect of an end-mass on a beam damping, *Experimental Mechanics* 9 (1989) 336–341.
[23] G.G. Wren, V.K. Kinra, Modeling and measurement of axial and flexural damping in metal-matrix composites, *Mechanics and Mechanisms of Material Damping*, vol. 1169, American Society for Testing and Materials, 1992, pp. 282–315.
[24] G.G. Wren, V.K. Kinra, Flexural damping of a P55 graphite magnesium composite, *Journal of Materials Science* 30 (1995) 3279–3284.
[25] J.E. Bishop, V.K. Kinra, Some improvements in the flexural damping measurement techniques, *Mechanics and Mechanisms of Material Damping*, vol. 1169, American Society for Testing and Materials, 1992, pp. 457–470.
[26] I.C. Finegan, R.F. Gibson, Recent research on enhancement of damping in polymer composite, *Composite Structures* 44 (1999) 89–98.
[27] R.F. Gibson, Damping characteristics of composites materials and structures, *Journal of Materials Engineering and Performance* 1 (1992) 11–20.
[28] Z. Zhang, G. Hartwig, Relation of damping and fatigue damage of unidirectional fibre composite, *International Journal of Fatigue* 24 (2002) 713–718.
[29] D. Ouis, Effect of structural defects on the strength and damping properties of a solid material, *European Journal of Mechanics A/Solids* 22 (2003) 47–54.
[30] Z. Xu, M.Y. Wang, T. Chen, An experimental study of particle damping for beams and plates, *Journal of Vibration and Acoustics* 126 (2004) 141–148.
[31] J.L. Ha, R.F. Fung, S.H. Chang, Quantitative determination of material viscoelasticity using a piezoelectric cantilever bimorph beam, *Journal of Sound and Vibration* 289 (2006) 529–550.
[32] N. Srikanth, M. Gupta, Damping characterization of magnesium based composites using an innovative circle-fit approach, *Composites Science and Technology* 63 (2003) 559–568.
[33] R.F. Gibson, R. Plunkett, Dynamic behavior of fiber-reinforced composites: measurements and analysis, *Journal of Composite Materials* 10 (1976) 325–332.
[34] V. Jiejun, L. Chenggong, W. Dianbin, G. Manchang, Damping and sound absorption properties of particle Al matrix composite foams, *Composites Science and Technology* 63 (2003) 569–574.
[35] N.W. Tschoegl, W.G. Knauss, I. Emri, Poisson's ratio in linear viscoelasticity—a critical review, *Mechanics of Time-Dependent Materials* 6 (2002) 3–51.
[36] M.E. McIntyre, J. Woodhouse, On measuring the elastic and damping constants of orthotropic sheet materials, *Acta Metallurgica* 36 (6) (1988) 1397–1416.
[37] J.P. Talbot, J. Woodhouse, The vibration damping of laminated plates, *Composites Part A* 28 (1997) 1007–1012.
[38] J. De Visscher, H. Sol, W.P. De Wilde, J. Vantomme, Identification of the damping properties of orthotropic composite materials using a mixed numerical experimental method, *Applied Composite Materials* 4 (1997) 13–33.
[39] M. Matter, T. Gmür, J. Cugnoni, A. Schorderet, Numerical-experimental identification of the elastic and damping properties in composite plates, *Composite Structures* 90 (2009) 180–187.
[40] A. Giraudeau, F. Pierron, Identification of stiffness and damping properties of thin isotropic plates using the virtual fields method: theory and simulations, *Journal of Sound and Vibration* 284 (3–5) (2005) 757–781.
[41] A. Giraudeau, B. Guo, F. Pierron, Stiffness and damping identification from full-field measurements on vibrating plates, *Experimental Mechanics* 46 (6) (2006) 777–787.
[42] S. Avril, M. Grédiac, F. Pierron, Sensitivity of the virtual fields method to noisy data, *Computational Mechanics* 34 (6) (2004) 439–452.
[43] M. Geradin, D. Rixen, *Mechanical Vibrations: Theory and Application to Structural Dynamics*, second ed, Wiley, New York, 1997.
[44] S. Avril, F. Pierron, General framework for the identification of constitutive parameters from full-field measurements in linear elasticity, *International Journal of Solids and Structures* 44 (2007) 4978–5002.
[46] R. Moulart, F. Pierron, S. Hallett, M. Wisnom, Full-field strain measurements at high rate on notched composites tested with a tensile hopkinson bar, *SEM Annual Conference on Experimental Mechanics*, Society for Experimental Mechanics, Albuquerque, New Mexico, USA, 1–4 June 2009.
[47] I. Doghri, *Mechanics of Deformable Solids*, Springer, Berlin, 2000.
[48] D. Jones, *Viscoelastic Vibration Damping*, Wiley, New York, 2001.
[49] M. Grédiac, E. Toussaint, F. Pierron, Special virtual fields for the direct determination of material parameters with the virtual fields method. 1—Principle and definition, *International Journal of Solids and Structures* 39 (10) (2000) 2691–2705.
[50] M. Grédiac, E. Toussaint, F. Pierron, Special virtual fields for the direct determination of material parameters with the virtual fields method. 3—Application to the bending rigidities of anisotropic plates, *International Journal of Solids and Structures* 40 (10) (2003) 2401–2419.
[51] E. Toussaint, M. Grédiac, F. Pierron, The virtual fields method with piecewise virtual fields, *International Journal for Mechanical Sciences* 48 (3) (2006) 256–264.
[52] K. Syed-Muhammad, E. Toussaint, M. Grédiac, S. Avril, J.H. Kim, Characterization of composite plate using the virtual fields method with optimized loading conditions, *Composite Structures* 85 (2008) 70–82.
[53] S. Rao, *The Finite Element Method in Engineering*, fourth ed, Elsevier, Amsterdam, 2005.
[54] O.C. Zienkewicz, R.L. Taylor, The finite element method, *The Basis*, vol. 1, fifth ed., Butterworth-Heinemeann, 2000.
[55] J. Gittus, *Creep, Viscoelasticity and Creep Fracture in Solids*, Applied Science Publishers Ltd, London, 1975.
[56] J. Lemaitre, J.-L. Chaboche, *Mechanics of Solids Materials*, Springer, Berlin, 1990.
[57] Y. Surrel, Deflectometry: a simple and efficient non interferometric method for slope measurement, *SEM Annual Congress on Experimental Mechanics*, Society for Experimental Mechanics, Costa Mesa, California, USA, 7–10 June 2004.
[58] Y. Surrel, Customized phase shift algorithms, *Elsevier Science*, January 2000, pp. 71–83.
[59] T. Pritz, Measurement methods of complex poisson's ratio of viscoelastic materials, *Applied Acoustics* 60 (2002) 279–292.